Noninvasive MRI native T_1 mapping detects response to *MYCN*-targeted therapies in the Th-*MYCN* model of neuroblastoma

Konstantinos Zormpas-Petridis[1], Evon Poon[2], Matthew Clarke[3], Neil P. Jerome[1,4,5], Jessica K.R. Boult[1], Matthew D. Blackledge[1], Fernando Carceller[2,6], Alexander Koers[2], Giuseppe Barone[6], Andrew D.J. Pearson[2], Lucas Moreno[8], John Anderson[7,9], Neil Sebire[9,10], Kieran McHugh[11], Dow-Mu Koh[1], Louis Chesler[2], Yinyin Yuan[3], Simon P. Robinson[1] and Yann Jamin[1,*].

[1] Division of Radiotherapy and Imaging, The Institute of Cancer Research, London and The Royal Marsden NHS Trust, 15 Cotswold Rd. Belmont, Sutton, Surrey SM2 5NG, United Kingdom.

[2] Division of Clinical Studies, The Institute of Cancer Research, London and The Royal Marsden NHS Trust, 15 Cotswold Rd. Belmont, Sutton, Surrey SM2 5NG, United Kingdom.

[3] Division of Molecular Pathology, The Institute of Cancer Research, London and The Royal Marsden NHS Trust, 15 Cotswold Rd. Belmont, Sutton, Surrey SM2 5NG, United Kingdom.

[4] Department of Circulation and Medical Imaging, Norwegian University of Science and Technology (NTNU), Trondheim, Norway

[5] Clinic of Radiology and Nuclear Medicine, St. Olavs Hospital, Trondheim, Norway

[6] Children & Young People's Unit, The Royal Marsden NHS Foundation Trust, Downs Rd, Sutton, SM2 5PT, United Kingdom.

[7] Department of Pediatric Oncology, Great Ormond Street Hospital for Children, London WC1N 3JH, United Kingdom

[8] Pediatric Hematology & Oncology, Hospital Universitari Vall d'Hebron, Barcelona, Spain.

[9] Institute of Child Health, University College London, London WC1N 1EH, UK

[10] Department of Pathology, Great Ormond Street Hospital for Children, London WC1N 3JH, United Kingdom

[11] Department of Radiology, Great Ormond Street Hospital for Children, London WC1N 3JH, United Kingdom

Research Article

Running title*:* T_1-mapping of neuroblastoma histopathology

Keywords: Spin lattice relaxation T_1, apoptosis, imaging biomarkers, pediatric cancer

Financial support: Y. Jamin received a Children with Cancer UK Research Fellowship (2014/176). Y. Jamin and S.P. Robinson received Rosetrees Trust grant M593. S.P. Robinson received Cancer Research UK grant C16412/A27725. E. Poon and L. Chesler received Children with Cancer UK Project Grant (2014/174). F.Carceller is partly supported by George and Giant Pledge via the Royal Marsden Cancer Charity. L. Chesler received Cancer Research UK Program Grant (C34648/A18339 and C34648/A14610). J. Anderson received a GOSHCC research leadership award. This work was supported in part by a Cancer Research UK and EPSRC to the Cancer Imaging Centre at ICR, in association with the MRC and Department of Health (England) (C1060/A10334 and C1060/A16464), the NIHR GOSH Biomedical Research Centre, the Oak Foundation to the Royal Marsden.

Corresponding author:
Dr. Yann Jamin,
Centre for Cancer Imaging,
Division of Radiotherapy and Imaging,
The Institute of Cancer Research, London and Royal Marsden NHS Foundation,
15 Cotswold Road, Sutton, Surrey, SM2 5NG, United Kingdom.
Email: Yann.Jamin@icr.ac.uk
Tel: +44 20 8722 4992
Fax: +44 20 8661 0846

Conflict of interest: The authors have no conflict of interest to disclose.

Word count: 4323

Number of tables: 3

Number of figures: 6

Abstract (245 words)

Noninvasive early indicators of treatment response are crucial to the successful delivery of precision medicine in children with cancer. Neuroblastoma is a common solid tumor of young children that arises from anomalies in neural crest development. Therapeutic approaches aiming to destabilize *MYCN* protein, such as small molecule inhibitors of Aurora A and mTOR, are currently being evaluated in early phase clinical trials in children with high-risk *MYCN*-driven disease, with limited ability to evaluate conventional pharmacodynamic biomarkers of response. T_1 mapping is an MRI scan that measures the proton spin-lattice relaxation time T_1. Using a multiparametric MRI-pathological cross-correlative approach and computational pathology methodologies including a machine learning-based algorithm for the automatic detection and classification of neuroblasts, we show here that T_1 mapping is sensitive to the rich histopathological heterogeneity of neuroblastoma in the Th-*MYCN* transgenic model. Regions with high native T_1 corresponded to regions dense in proliferative undifferentiated neuroblasts, whereas regions characterized by low T_1 were rich in apoptotic or differentiating neuroblasts. Reductions in tumor native T_1 represented a sensitive biomarker of response to treatment-induced apoptosis with two *MYCN*-targeted small molecule inhibitors: Aurora A kinase inhibitor alisertib (MLN8237) and MTOR inhibitor vistusertib (AZD2014). Overall, we demonstrate the potential of T_1-mapping, a scan readily available on most clinical MRI scanners, to assess response to therapy and guide clinical trials for children with neuroblastoma. The study reinforces the potential role of MRI-based functional imaging in delivering precision medicine to children with neuroblastoma.

Significance

This study shows that MRI-based functional imaging can detect apoptotic responses to *MYCN*-targeted small molecule inhibitors in a genetically-engineered murine model of *MYCN*-driven neuroblastoma.

Introduction

Neuroblastoma is a tumor arising from anomalies in the embryonic sympatho-adrenal lineage of the neural crest in children (1). Despite intensive frontline multimodal therapy, neuroblastoma still accounts for 13% of all cancer-related deaths in children due to resistant, relapsing and systemic disease. Promising novel targeted therapeutic approaches against neuroblastoma are being developed and include small-molecule inhibitors as well as epigenetic, noncoding-RNA, and cell-based immunologic therapies (2-5). Amplification of the proto-oncogene *MYCN* is the most common genomic aberration, which defines a subgroup of children with a high-risk disease. *MYCN* plays a central role in the biology of high-risk neuroblastoma and as such represents a major therapeutic target.

The application of the mouse hospital and co-clinical trial concept represents a clear paradigm shift in neuroblastoma translational research (2,6). This approach integrates more advanced mouse modelling, including genetically-engineered mouse (GEM) models, such as the Th-*MYCN* mouse (7), to accelerate the discovery and evaluation of novel therapeutic strategies, and helps shape the clinical trial pipeline priorities for children with high-risk disease. Small molecule inhibitors targeting the stability of MYCN protein have shown strong anti-tumor activity in the Th-*MYCN* model and are being evaluated in early-phase pediatric clinical trials (2,8-10). These include the selective inhibitor of Aurora A kinase, alisertib (MLN8237, NCT01601535), and selective inhibitors of mTOR activity (NCT01331135, NCT01467986, NCT01625351, NCT02343718, NCT02574728, NCT02638428, NCT02813135).

Evaluation of response to treatment in children with neuroblastoma is based on Response Evaluation Criteria in Solid Tumours (RECIST) using non-invasive anatomical imaging such as computed tomography (CT) or magnetic resonance imaging (MRI). The revised International Neuroblastoma Response Criteria (INRC) guidelines now also include sensitive nuclear medicine-based functional imaging approaches such (metaiodobenzylguanidine [MIBG] scans and [F-18]2-fluoro-2-deoxyglucose positron emission tomography/CT [FDG PET/CT]) for the assessment of bone and bone marrow metastatic disease, present in 50% of cases (11). In addition to providing more accurate detection of active disease, functional imaging techniques may also provide biomarkers of response to novel therapies in neuroblastoma clinical trials, in which conventional pharmacodynamic biomarkers can be difficult to evaluate. MRI is becoming the preferred clinical imaging technique for the management of children with neuroblastoma because of

its exquisite soft tissue contrast. MRI provides excellent anatomical information at diagnosis and follow up while sparing exposure to ionising radiation associated with CT. Advanced MRI-based functional imaging techniques can be used to define quantitative imaging biomarkers that inform on biologically relevant structure-function relationships in pediatric cancers *in vivo* (12).

The mouse hospital concept provides a unique opportunity to evaluate predictive and prognostic imaging biomarkers of response in neuroblastoma and to perform the close imaging-pathology correlation necessary to understand the biological processes underpinning the imaging measurement and provide the stringent validation needed before they can be deployed clinically. We have previously demonstrated that a reduction in the tumor native spin-lattice relaxation time T_1, measured using inversion recovery true fast imaging with steady-state precession (IR-TrueFISP) MRI, can provide a sensitive biomarker of response to cyclophosphamide, which is a usual component of various frontline protocols for neuroblastoma, and anti-vascular therapies in the Th-*MYCN* model (13).

In this study we evaluate how a reduction in native tumor T_1 provides a robust biomarker of response to alisertib and the mTOR inhibitor vistusertib (AZD2014) in the Th-*MYCN* model. By comparing native T_1 maps with those derived from multi-parametric MRI and computational pathology, we demonstrate that native T_1 mapping (the voxel-wise quantification of T_1) is sensitive to the rich histological presentation of neuroblastoma, including regional differences in undifferentiated, differentiating and apoptotic neuroblast density. This study demonstrates the potential application of T_1 mapping for diagnosis/prognosis, surgical planning and the evaluation of novel therapies for children with neuroblastoma.

Materials and Methods

Animals, imaging and drug treatment schedule

All experiments were performed in accordance with the local ethical review panel, the UK Home Office Animals (Scientific Procedures) Act 1986, the United Kingdom National Cancer Research Institute guidelines for the welfare of animals in cancer research (14) and the ARRIVE (animal research: reporting in vivo experiments) guidelines (15).

Transgenic Th-*MYCN* mice were genotyped to detect the presence of the human *MYCN* transgene (7). The study was performed using both male and female homozygous mice, which developed a single palpable abdominal tumor at 40–80 days old with 100% penetrance. Tumor development was monitored weekly by palpation by an experienced animal technician. A total of 46 mice were enrolled with a median tumor volume of 861 ± 86 mm^3 (derived from T_2-weighted MRI; median ± 1 s.e.m., ranging from 280 to 2557 mm^3). MRI was performed prior to treatment (*Day 0*). Mice were left to recover for 24h, and then treated (*Day 1)* with 30 mg/kg p.o. of Alisertib (MLN8237, purchased from Selleckchem, n=11) or vehicle (10% 2-hydroxypropyl β-cyclodextrin, 1% $NaHCO_3$, n=9), or 25 mg/kg p.o. of Vistusertib (AZD2014, obtained under material transfer agreement with AstraZeneca, n=14) or vehicle (5% DMSO, 95% PEG300, n=12). Post treatment MRI was performed 24h after treatment started (*Day 2*). Mice were housed in specific pathogen-free rooms in autoclaved, aseptic microisolator cages (maximum of 4 mice per cage) and allowed access to sterile food and water *ad libitum*.

MRI

All MRI studies were performed on a 7T Bruker horizontal bore MicroImaging system (Bruker Instruments, Ettlingen, Germany) using a 3cm birdcage volume coil. Anesthesia was induced by an intraperitoneal 5ml/kg injection of a combination of fentanyl citrate (0.315mg/ml) plus fluanisone (10mg/ml) (Hypnorm, Janssen Pharmaceutical, Oxford, UK) and midazolam (5mg/ml) (Roche, Welwyn Garden City, UK) and water (1:1:2). Core temperature was maintained at ~37°C with warm air blown through the magnet bore.

For all the mice, contiguous anatomical T_2-weighted transverse images were acquired through the mouse abdomen for the quantification of tumor volume, optimization of the local field homogeneity using the FASTmap algorithm, and for planning the subsequent multiparametric MRI measurements. In addition to IR-TrueFISP MRI for quantification of the spin-lattice (T_1) and spin-spin (T_2) relaxation times, these also included measurement of the

apparent diffusion coefficient (ADC), the transverse relaxation rate R_2* and the magnetization transfer ratio (MTR) using the MRI sequences and parameters listed in Supplementary Table 1.

Tumor volumes were determined using segmentation from regions of interest drawn on each tumor-containing T_2-weighted MRI slice using OsiriX. All the multiparametric MRI data were fitted voxelwise using in-house software (ImageView, working under IDL, ITT, Boulder, Colorado, USA) with a robust Bayesian approach that provided estimates of T_1, T_2, ADC and R_2*. MTR (%) was calculated as $MTR= (1-M_{25ppm}/M_{100ppm})*100$ and fitted voxelwise using in-house code written in Matlab (The Mathworks, Natick, MA).

Computational pathology/digital pathology

Digitized histology. Guided by T_2-weighted MRI, tumors were carefully excised and orientated for histopathological processing. Formalin-fixed and paraffin-embedded tumors were sectioned (3µm) and stained with hematoxylin and eosin (H&E). Wholeslide H&E images were digitized using a Hamamatsu NanoZoomer XR scanner (20x magnification, 0.46µm resolution, Hamamatsu, Japan). Histology images were subsequently split into tiles of 2000x2000 pixels (jpeg) for computational efficiency using Bio-Formats (https://www.openmicroscopy.org/bio-formats/).

MRI-histology alignment. For each tumor, the MRI slice of interest was visually aligned with the digitized whole-slide H&E stained image using anatomical landmarks as recently described (16).

Cell segmentation and classification. Image processing was carried out using CRImage (17). First, cell nuclei were extracted from H&E-staining by Otsu thresholding (18). Noisy image structures were then deleted using morphological opening. The clustered nuclei were separated by the Watershed algorithm. For every nucleus, 91 morphological (19), three local-context and 46 cell-cytoplasm features were extracted. A support vector machine (SVM) with a radial basis function (RBF, γ=1/number_of_features) kernel was trained with these features, based on annotations provided by a neuropathologist on 16320 cells from 7 whole-slide samples. Cells were subsequently classified into 5 categories: undifferentiated neuroblasts, differentiating neuroblasts, apoptotic cells, lymphocytes, stromal cells.

Generation of cellular density and classified cell parametric maps. Whole-slide images of cells were processed to match the MRI resolution (234 x 234 μm), with the number of segmented cells and classified cells within 518x518 pixel-regions representing a single pixel in the final cell density maps. Density maps were normalized to their sample's maximum number of cells/classified cells in order to facilitate the evaluation intra-tumor heterogeneity.

MRI- and histology-derived parametric map registration. This was performed as recently described using the automatic coherent point drift (CPD) algorithm (16,20). Firstly, density maps of all the segmented cells were non-rigidly registered to the T_1 images based on features extracted by a Canny edge detector. The same transformation was subsequently applied to the density maps of each classified cell category.

Spatial quantitative comparison between MRI parametric maps or between MRI- and histology-derived maps. The first parametric maps were divided into sub-regions of high and low values using thresholds summarized in Supplementary Table 2. A binary mask was created for each sub-region and applied to the second parametric map. This analysis was performed in 13 tumors across both vehicle cohorts for which precise MRI-Pathology registration was possible. Statistical comparison of sub-regional median values between the two parametric maps was performed and the process was repeated in reverse.

Statistical Analysis

Statistical analysis was performed with GraphPad Prism 7 (GraphPad Software Inc., La Jolla, USA). The mean values for tumor volume, and the mean of the median values for all the quantitative MRI parameters were used. All the absolute and treatment-induced relative changes in MRI parameters were assumed to be normally distributed, which was confirmed using the D'Agostino-Pearson omnibus K2 normality test. Student's two-tailed t-test was used to assess any significant differences in quantitative MRI parameters and tumor volume upon treatment (paired), and in the magnitude of these changes compared to the control cohort (unpaired), with a 1% level of significance. Further statistical analysis was performed with the Bonferroni correction (n=5). Any significant differences between groups identified in the sub-regional analysis were identified using the Wilcoxon signed rank test with a 5% level of significance. Significant correlations were determined using linear regression analysis, confirmed by using the robust regression and outlier removal approach (21).

Results

Alisertib and vistusertib elicit significant anti-tumor activity associated with a decrease in native T_1.

The Th-*MYCN* GEM model of neuroblastoma recapitulates the aggressiveness of the clinical disease, with an observed average 31 ± 4% increase in tumor volume measured over the 48h experimental timecourse (Table 1A&B, Fig. 1). Despite this, tumor median values for all the MRI parameters remained stable over 48h in the vehicle treated cohorts (coefficients of variation CoV_{T_1}= 2.4%, CoV_{T_2}= 5.8%, CoV_{ADC}= 14.0%, CoV_{R_2*}= 11.7%, CoV_{MTR}= 6.2%). There was no significant difference in tumor volume between the different treatment cohorts at the time of enrollment (Supplementary Fig. S1). Treatment with either alisertib or vistusertib led to a highly significant reduction in native T_1 (-9.3 ± 0.9% and -5.4 ± 1.1%, both P<0.0001) and was associated with a significant reduction in tumor volume with vistusertib (-42 ± 5.1%, P<0.0001) but not alisertib, although a reduction in tumor volume was seen in 9 out of 11 treated mice (Supplementary Fig. S2A&B). Both the alisertib and vistusertib treated groups elicited significant anti-tumor activity when compared to their respective vehicle control cohorts (both P<0.0001). No significant changes in tumor native T_2, ADC, R_2*, or MTR were determined following treatment with either alisertib or vistusertib, nor any treatment-induced relative changes compared with vehicle controls.

Low native tumor T_1 correlates with high tumor red blood cell content.

Tumors arising in the Th-*MYCN* model present a characteristically hemorrhagic phenotype with large areas of extravasated red blood cells (RBC). The transverse relaxation rate R_2* is sensitive to the concentration of paramagnetic deoxyhemoglobin associated with deoxygenated RBCs, hence neuroblastomas typically exhibit relatively high R_2* values. We recently validated R_2* as a robust biomarker for mapping RBC distribution in this tumor model (16).

Visual comparison of native T_1 and R_2* maps (Fig. 1) showed that regions of high R_2* co-localized with regions of low native T_1. Retrospective analysis of measurements made in 71 untreated tumors arising in GEM models of neuroblastoma (Supplementary Methods) revealed that the median native T_1 inversely correlated with native median R_2* (r= *-0.59, P<0.0001*) (Fig. 2A). Sub-regional analysis using established empirical R_2* threshold values (R_2*< 70s^{-1} as no hemorrhage (16,22) and > 200s^{-1} as purely RBC, and mixed regions of

neuroblasts and RBC for the R_2* values between) identified significantly different values of T_1 associated with low (<70s^{-1}), intermediate and high (>250s^{-1}) R_2* (Fig. 2B). Comparison of the relative changes in median T_1 and R_2* with treatment revealed a significant negative correlation (r = -0.78, P = 0.002 with Bonferroni correction [n=5], Fig. 2C). Importantly, both positive and negative changes in tumor R_2* occurred with treatment, thereby accentuating the sensitivity of native T_1 to RBC deposition, but excludes changes in the content of paramagnetic RBCs or other such species as the main cause of reduction in T_1 upon treatment.

High native tumor T_1 correlates with high density of undifferentiated neuroblasts and with low density of apoptotic neuroblasts.

We then focused on the major histological component of these tumors, i.e the dense cellular network. We trained a cell classifier, which allowed the robust segmentation and classification of five different classes of cells with an overall accuracy of 95.3% (Fig. 3A&B, confusion matrix shown in Supplementary Table 3, Supplementary Fig. 3A&B). We generated parametric maps of undifferentiated neuroblasts and apoptotic cells density and compared them with spatially-registered native T_1 maps. In vehicle control tumors, regions exhibiting high values of T_1 co-localized with dense regions of undifferentiated neuroblasts (Fig. 4). Threshold-based sub-regional analysis confirmed that regions with higher T_1 values corresponded to areas of increased density of undifferentiated neuroblasts and, reciprocally, regions with higher neuroblast density had higher native T_1 values (Fig. 5A&B and Supplementary Table 2). Interestingly, areas dense in apoptotic cells in vehicle control tumors also corresponded to regions of lower native T_1. The widespread reduction in T_1 seen in the vistusertib-treated tumors was associated with a widespread and significantly higher fraction of apoptotic cells (57 ± 3% compared to 16 ± 3% in vehicle control, P<0.0001) and tissue damage, concomitant with a significantly lower fraction of undifferentiated neuroblasts (21 ± 3% compared to 64 ± 4% in vehicle control, P<0.0001) (Fig. 5C). The more modest but widespread reduction in T_1 in the alisertib-treated tumors was not associated with any detectable differences in the fraction of apoptotic or undifferentiated neuroblasts on corresponding H&E staining, as confirmed by cleaved caspase 3 staining (Supplementary Fig. S4). Note that this response was however associated with the reduction in tumor volume seen in 9 out of the 11 mice treated (Supplementary Fig. S2), and the absence of any significant difference in tumor T_1 post-treatment between the alisertib and vehicle control cohorts (contrary to that seen with vistusertib, P<0.0001).

Combining the MRI data from vistusertib and alisertib treated mice with matched histopathology revealed a significant negative correlation between treatment-induced reduction in T_1 over 24h and the proportion of apoptotic neuroblasts present in the tumour at the study endpoint (r= -0.55, P=0.04, Fig. 5D). Combining the MRI data from vehicle control, vistusertib and alisertib-treated tumors with matched histopathology showed a positive correlation between median T_1 and the ratio of undifferentiated neuroblasts (r= 0.70, P<0.0001, Fig. 5E) and a negative correlation with the fraction of apoptotic cells (r=-0.63, P=0.006, Fig. 5F).

Regions rich in differentiating neuroblasts are associated with lower T_1 values.

We identified three tumors exhibiting a significant amount of differentiating neuroblasts (yet with only very few mature ganglion cells). In these tumors (Fig. 6), previously shown to have very low levels of hemorrhage (16), regional differences in T_1 visually and spatially corresponded to differences in undifferentiated neuroblast density, with regions of low T_1 and low density undifferentiated neuroblasts corresponding to hotspots of differentiating neuroblasts, arranged in islands separated by a large amount of neuropil or simply interspersed with undifferentiated neuroblasts.

Discussion

In pediatric oncology, the difficulty of obtaining post-therapy surgical biopsies is hindering the development of robust predictive/prognostic pharmacodynamic biomarkers of response urgently needed to accelerate the clinical evaluation of more effective and safer therapeutic strategies. Recent large molecular profiling protocols at national level (23-25), advocate for biopsies at the time of relapse in order to identify actionable alterations in pediatric recurrent cancers. In this regard, advanced MRI-based functional imaging techniques that can define quantitative biomarkers to noninvasively visualise spatial variations and temporal evolution of tissue structure-function *in vivo* are being actively explored (12). Early imaging biomarker development demands close imaging-pathology correlation, to understand the biological processes underpinning the imaging measurement, before they can be routinely deployed in the clinic (26).

In this study we demonstrate how T_1 mapping is sensitive to the rich histological presentation of neuroblastoma, and can provide a sensitive biomarker of response to two clinically-relevant *MYCN*-targeted therapeutics in the Th-*MYCN* GEM model of neuroblastoma. We have continued to exploit computational pathology methodologies to enable the precise comparison of MRI parametric maps with whole-slide digitized pathology (16). Importantly, the Th-*MYCN* GEM model recapitulates the chemosensitivity and patho-physiology of high-risk, *MYCN*-amplified neuroblastoma, including a dense and hemorrhagic vascular phenotype and undifferentiated or poorly differentiated tumor phenotype with a high mitosis-karyorrhexis index, indicative of both a high level of proliferation and apoptosis (27).

T_1 mapping of neuroblastoma histopathology and its regional heterogeneity

Using this approach, we have identified, and confirmed using quantitative sub-regional analysis, four major determinants of the regional heterogeneity observed on native T_1 maps: *i)* regions with high T_1 values corresponded to hotspots of undifferentiated neuroblasts, characterized by a high level of proliferation, whereas *ii)* regions rich in differentiating neuroblasts exhibited lower T_1 values, and both *iii)* regions with large amounts of extravasated RBCs and *iv)* large areas of cell damage, with or without RBCs, were both associated with very low T_1 values. The association between T_1 and extravasated RBCs was an expected finding consistent with the linear relationship of blood T_1 with hematocrit level and hemorrhage (28).

Reduction in tumor native T_1 is associated with a reduction in undifferentiated neuroblast density

Our data with vistusertib indicates that the reduction in native T_1 was associated with a shift in tumor composition characterized by rapid loss of tumor regions with higher T_1 values, a consequence of cell death, with the post-therapy tumor T_1 values determined by dying and remaining hemorrhagic fractions. A similar conclusion can be drawn on the contrast mechanism underpinning the reduction in T_1 upon treatment with alisertib, based on both the known mechanism of response to alisertib through apoptosis in this model and the observed reduction in tumor volume in our study (10). However we could not confirm this using endpoint histopathological assessment, potentially due to the high inter-tumor heterogeneity both in terms of the amount of apoptosis present at the time of enrollment (as shown by the endpoint histopathology in the vehicle cohorts) and in the actual response to alisertib treatment in this model as recently reported (10). The absence of any significant relative change in R_2*, a validated biomarker for RBCs (29), or T_2, ADC and MTR, which all relate to tissue water content/binding, strongly suggests that the overall decrease in T_1 is being driven by the loss of the tissue fraction with high T_1 values, i.e. regions with a high density of undifferentiated neuroblasts, rather than a gain of new MRI contrast e.g. that resulting from cell death-mediated release of paramagnetic ions (30,31).

Why is T_1 sensitive to neuroblastoma histopathology and its modulation?

By definition, the spin-lattice T_1 relaxation time refers to the interaction or energy transfer between the excited ^{1}H spin and the molecules within the surrounding molecular structure. The T_1 value, i.e. the efficacy of the spin-lattice relaxation, is dependent on molecular tumbling of the molecule in which the proton resides. For MRI applications, this molecule is primarily water, which can be present in three states associated with different T_1 values: *i)* free water (free to move, high T_1), *ii)* "structured" water (bound to a macromolecule by a single bond where molecular tumbling is still possible, lower T_1), *iii)* "bound" water (found in solids, bound by multiple bonds, high T_1). The general consensus is that the reduced tissue T_1 of structured water is a consequence of its interaction with proteins and other macromolecules. Tissue T_1 thus depends on compartmentalization of structured water and the amount of molecular crowding within each different compartment. Cancer cells and tumor tissue typically have elevated T_1 values compared to normal tissues, the original observation that demonstrated the potential of MRI for cancer diagnosis. Elevated tumor T_1 remains attributed to a difference in intracellular water structure and order compared to

normal cells (32,33). T_1 has also been suggested to change during cell cycle and mitosis *in vitro*, a phenomenon also attributed to different levels of water-macromolecule interactions (34,35). However, very early work in MRI-detectable isolated large cells such as *Xenopus* oocytes and *Aplysia* neurons confirmed that cell nuclei exhibit higher T_1 values than the cytoplasm (1.85 vs 1.2s respectively for Xenopus oocytes at 7T), and that degradation/permeabilization of the nuclear envelope causes an equilibration of T_1 values (36,37). A more recent study reported anomalously rapid hydration water diffusion dynamics near DNA surfaces, which demonstrates that water interacts differently with DNA compared to protein. More precisely, water behaves like free water near DNA (38), which would explain both the higher nuclear T_1, and the change in T_1 observed during mitosis when the chromatin is condensed and DNA is less accessible to water molecules and the nuclear membrane completely disappears.

Poorly or undifferentiated neuroblastoma are defined as small round nuclei with stippled chromatin (diffuse open chromatin) with scant eosinophilic cytoplasm and indistinct cell borders. This definition is thus self-explanatory for the higher T_1 values reported here in areas of dense, undifferentiated neuroblasts (dense cells with a high nuclear/cytoplasmic ratio and minimal extracellular compartment). We can also assume that any reduction in undifferentiated cell density, or change in cell phenotype and/or intracellular compartmentalization, in a sufficiently large number of cells would thus result in a reduction in T_1 (39). The reduced native T_1 associated with dense areas of differentiating neuroblasts, characterized by lower nuclear to cytoplasmic ratio, lower cell density, and possibly surrounded by abundant eosinophilic neuropil, supports this hypothesis. Many of the events occurring during apoptosis, including water loss, pyknosis and karyorrhexis, would also align with a reduction in T_1 if happening in a sufficient number of cells (40). Interestingly, both pyknosis and karyorrhexis are steps common to apoptosis, necrosis and senescence, indicating a potential generic sensitivity of T_1 to cell death. As virtually all undifferentiated neuroblasts in this model are positive (and apoptotic cells negative) for the proliferation marker Ki67 (27), this hypothesis corroborates the studies by McSheehy and colleagues showing that a reduction in native T_1 positively correlates with Ki67 staining (30,31).

Potential further clinical applications in guiding risk stratification and surgical planning and early clinical trials to develop new drugs

The differential diagnosis and risk-stratification for children with neuroblastoma is based on criteria including histological features such as the grade of tumor differentiation. The sensitivity of T_1 mapping to regions rich in undifferentiated, apoptotic or differentiating

neuroblasts seen in the Th-*MYCN* model herein suggests its potential to noninvasively classify tumors by favorable and unfavorable histology. It may also help identify anaplastic lymphoma kinase (ALK) positive regions, mutations associated with poor outcome in neuroblastoma, and for which small molecule inhibitors are currently being developed. Interestingly, ALK mutations have been shown to be associated with a differentiating molecular signature, confirmed at a pathological level in several *MYCN*- and *ALK*-mutated GEM models (41-44). T_1 mapping may also afford additional prognostic value in confirmed cases of neuroblastoma, in which high cellular density of proliferative cells is associated with poor outcome, whereas a high density of apoptosis suggests a more favorable outcome (45). Finally, T_1 mapping may help identify the nature of tumors following the induction phase of frontline therapy, where it is uncertain if a mass is comprised of undifferentiated neuroblastoma or apoptotic or differentiated disease. In this regard, T_1-mapping would provide additional and complementary information to semi-quantitative molecular imaging strategies such as MIBG and FDG-PET scans and help confirm the nature and heterogeneity of the disease associated with MIBG avid/non-avid and FDG (positive/negative) disease. This is important as discrepancies exist between the expression of the norepinephrine transporter (NET), responsible for the uptake of MIBG, and the presence of an aggressive cellular phenotype. These include MIBG non-avid disease that presents in ~10% of children, and reduced NET protein expression in high risk MYCN-amplified disease (46). Additionally, targeted therapies against *MYCN* or *ALK* can lead to the modulation of vascular perfusion (and hence the delivery of radiolabeled MIBG and FDG), glucose uptake and NET expression, which may potentially lead to a change in MIBG avidity which does not reflect, or makes it difficult to assess, changes in the extent of active disease using the current INRC guidelines. Treatment with the histone deacetylase inhibitor Vorinostat has for example been shown to be effective against neuroblastoma while increasing NET transporter expression in neuroblastoma (47). T_1 mapping has the potential to help improve the accuracy of detection of active disease for enhance surgical tissue sampling, surgical resection planning and response assessment.

Translating T_1 mapping into the neuroblastoma clinic

The voxel-wise quantification of T_1 is an essential component of many MRI-based functional and molecular imaging techniques being developed to study the tumor microenvironment and for the evaluation of novel targeted therapies, including immunotherapy (48-53). DCE-MRI, arterial spin labelling (ASL-) MRI and oxygen-enhanced T_1-MRI are being evaluated clinically to assess tumor vascular perfusion/permeability and hypoxia. However, native

tumor T_1 maps acquired in the clinic are often only estimated and seldom reviewed or interpreted (13). In contrast, the clinical adoption of native T_1 mapping has increased the potential for the noninvasive and differential diagnosis of cardiac pathology (54,55) and the staging of chronic liver disease (56). The cardiac MR experience has shown that T_1 mapping is simple to perform and analyze, minimally subjective, and highly reproducible (~2% CoV for a modified Look-Locker inversion recovery MOLLI sequence over 24 hours (57)). However, there are many acquisition schemes available for T_1 mapping, and the measured T_1 will depend on the precision and reproducibility of each scheme, and how is it affected by motion, flow and off-resonance effects. In our study, one of the advantages of the IR-TrueFISP technique, aside from its high accuracy, is that it is inherently flow compensated in the directions of slice selection and readout, especially at the blood velocity observed in tumors (58), allowing us to exclude changes in vascular flow as a source of reduction in native T_1. Moving forward, including T_1-mapping in an ethically-approved clinical study within the standard-of-care frontline chemotherapy would provide the study to rapidly evaluate and validate T_1-mapping potential for the neuroblastoma clinic. Such a study would also inform on the potential of native T_1-mapping to help better define bone and bone marrow metastasis and its response to treatment.

Beyond neuroblastoma

The potential value of native T_1 reduction as a generic biomarker of early tumor response to therapy was first demonstrated by McSheehy and colleagues (30,31). By understanding the spatial relationship of T_1 mapping with regional variations in neuroblastoma phenotype, our study sheds new light into the biology underpinning native T_1 contrast, based on cell anatomy. Our data strongly supports the use of T_1 mapping as a generic approach to assess early response to cancer treatment, especially since *i)* the “small-blue-round-cell tumor” phenotype, characterized by monotonous proliferations of small, undifferentiated or poorly differentiated cells with scant cytoplasm, is actually used to refer to the phenotype of a large group of highly aggressive tumors, including many high-risk pediatric malignancies such rhabdomyosarcoma and medulloblastoma (and adult cancers such as certain subtypes of sarcoma, carcinoma, lymphoma, and melanoma) and *ii)* both pyknosis and karyorrhexis are common steps to the major cell death processes. However, it would be important to understand the disease or tissue-specific factors, which may also affect native T_1 including the presence of edema, fat or melanin.

In summary, our study demonstrates that native T_1 mapping can precisely and quantitatively map the rich histopathology of neuroblastoma tumors and its modulation by *MYCN*-targeted therapeutics in the clinically-relevant Th-*MYCN* model of neuroblastoma. By providing strong evidence for the sensitivity of native T_1 to dense areas of undifferentiated neuroblasts, our data suggest further application for diagnosis, risk stratification and surgical planning, and that its potential as a biomarker of successful response to therapy could be extended to larger subsets of aggressive pediatric and adult tumors. Widely available on conventional clinical scanners, our study provides a strong rationale for the incorporation of T_1 mapping both at the time of diagnosis and in early phase clinical trials to guide clinical decision making and the delivery of precision medicine to children with neuroblastoma.

References

1. Matthay KK, Maris JM, Schleiermacher G, Nakagawara A, Mackall CL, Diller L*, et al.* Neuroblastoma. Nat Rev Dis Primers **2016**;2:16078

2. Moreno L, Caron H, Geoerger B, Eggert A, Schleiermacher G, Brock P*, et al.* Accelerating drug development for neuroblastoma - New Drug Development Strategy: an Innovative Therapies for Children with Cancer, European Network for Cancer Research in Children and Adolescents and International Society of Paediatric Oncology Europe Neuroblastoma project. Expert Opin Drug Discov **2017**;12:801-11

3. Qadeer ZA, Valle-Garcia D, Hasson D, Sun Z, Cook A, Nguyen C*, et al.* ATRX In-Frame Fusion Neuroblastoma Is Sensitive to EZH2 Inhibition via Modulation of Neuronal Gene Signatures. Cancer Cell **2019**;36:512-27 e9

4. Xu X, Huang W, Heczey A, Liu D, Guo L, Wood M*, et al.* NKT Cells Coexpressing a GD2-Specific Chimeric Antigen Receptor and IL15 Show Enhanced In Vivo Persistence and Antitumor Activity against Neuroblastoma. Clin Cancer Res **2019**;25:7126-38

5. Zhao X, Li D, Yang F, Lian H, Wang J, Wang X*, et al.* Long Noncoding RNA NHEG1 Drives beta-Catenin Transactivation and Neuroblastoma Progression through Interacting with DDX5. Mol Ther **2020**;28:946-62

6. Clohessy JG, Pandolfi PP. Mouse hospital and co-clinical trial project--from bench to bedside. Nat Rev Clin Oncol **2015**;12:491-8

7. Weiss WA, Aldape K, Mohapatra G, Feuerstein BG, Bishop JM. Targeted expression of MYCN causes neuroblastoma in transgenic mice. EMBO J **1997**;16:2985-95

8. Mosse YP, Fox E, Teachey DT, Reid JM, Safgren SL, Carol H*, et al.* A Phase II Study of Alisertib in Children with Recurrent/Refractory Solid Tumors or Leukemia: Children's Oncology Group Phase I and Pilot Consortium (ADVL0921). Clin Cancer Res **2019**;25:3229-38

9. Vaughan L, Clarke PA, Barker K, Chanthery Y, Gustafson CW, Tucker E*, et al.* Inhibition of mTOR-kinase destabilizes MYCN and is a potential therapy for MYCN-dependent tumors. Oncotarget **2016**;7:57525-44

10. Brockmann M, Poon E, Berry T, Carstensen A, Deubzer HE, Rycak L*, et al.* Small molecule inhibitors of aurora-a induce proteasomal degradation of N-myc in childhood neuroblastoma. Cancer Cell **2013**;24:75-89

11. Park JR, Bagatell R, Cohn SL, Pearson AD, Villablanca JG, Berthold F*, et al.* Revisions to the International Neuroblastoma Response Criteria: A Consensus Statement From the National Cancer Institute Clinical Trials Planning Meeting. J Clin Oncol **2017**;35:2580-7

12. Manias KA, Gill SK, MacPherson L, Foster K, Oates A, Peet AC. Magnetic resonance imaging based functional imaging in paediatric oncology. Eur J Cancer **2017**;72:251-65

13. Jamin Y, Tucker ER, Poon E, Popov S, Vaughan L, Boult JK*, et al.* Evaluation of clinically translatable MR imaging biomarkers of therapeutic response in the TH-MYCN transgenic mouse model of neuroblastoma. Radiology **2013**;266:130-40

14. Workman P, Aboagye EO, Balkwill F, Balmain A, Bruder G, Chaplin DJ*, et al.* Guidelines for the welfare and use of animals in cancer research. Br J Cancer **2010**;102:1555-77

15. Kilkenny C, Browne WJ, Cuthill IC, Emerson M, Altman DG. Improving bioscience research reporting: the ARRIVE guidelines for reporting animal research. PLoS Biol **2010**;8:e1000412

16. Zormpas-Petridis K, Jerome NP, Blackledge MD, Carceller F, Poon E, Clarke M*, et al.* MRI Imaging of the Hemodynamic Vasculature of Neuroblastoma Predicts Response to Antiangiogenic Treatment. Cancer Res **2019**;79:2978-91

17. Pau G, Fuchs F, Sklyar O, Boutros M, Huber W. EBImage—an R package for image processing with applications to cellular phenotypes. Bioinformatics **2010**;26:979-81

18. Otsu N. A threshold selection method from gray-level histograms. IEEE transactions on systems, man, and cybernetics **1979**;9:62-6

19. Yuan Y, Failmezger H, Rueda OM, Ali HR, Gräf S, Chin S-F*, et al.* Quantitative image analysis of cellular heterogeneity in breast tumors complements genomic profiling. Science translational medicine **2012**;4:157ra43-ra43

20. Myronenko A, Song X. Point set registration: Coherent point drift. Ieee T Pattern Anal **2010**;32:2262-75

21. Motulsky HJ, Brown RE. Detecting outliers when fitting data with nonlinear regression - a new method based on robust nonlinear regression and the false discovery rate. BMC bioinformatics **2006**;7:123

22. Jamin Y, Glass L, Hallsworth A, George R, Koh DM, Pearson AD*, et al.* Intrinsic susceptibility MRI identifies tumors with ALKF1174L mutation in genetically-engineered murine models of high-risk neuroblastoma. PLoS One **2014**;9:e92886

23. George SL, Izquierdo E, Campbell J, Koutroumanidou E, Proszek P, Jamal S*, et al.* A tailored molecular profiling programme for children with cancer to identify clinically actionable genetic alterations. Eur J Cancer **2019**;121:224-35

24. Ackermann S, Cartolano M, Hero B, Welte A, Kahlert Y, Roderwieser A*, et al.* A mechanistic classification of clinical phenotypes in neuroblastoma. Science **2018**;362:1165-70

25. Massard C, Michiels S, Ferte C, Le Deley MC, Lacroix L, Hollebecque A*, et al.* High-Throughput Genomics and Clinical Outcome in Hard-to-Treat Advanced Cancers: Results of the MOSCATO 01 Trial. Cancer Discov **2017**;7:586-95

26. O'Connor JP, Aboagye EO, Adams JE, Aerts HJ, Barrington SF, Beer AJ*, et al.* Imaging biomarker roadmap for cancer studies. Nat Rev Clin Oncol **2017**;14:169-86

27. Moore HC, Wood KM, Jackson MS, Lastowska MA, Hall D, Imrie H*, et al.* Histological profile of tumours from MYCN transgenic mice. J Clin Pathol **2008**;61:1098-103

28. Lu H, Clingman C, Golay X, Van Zijl PC. Determining the longitudinal relaxation time (T1) of blood at 3.0 Tesla. Magnetic Resonance in Medicine: An Official Journal of the International Society for Magnetic Resonance in Medicine **2004**;52:679-82

29. Acerbi I, Cassereau L, Dean I, Shi Q, Au A, Park C*, et al.* Human breast cancer invasion and aggression correlates with ECM stiffening and immune cell infiltration. Integ Biol **2015**;7:1120-34

30. McSheehy PM, Weidensteiner C, Cannet C, Ferretti S, Laurent D, Ruetz S*, et al.* Quantified tumor t1 is a generic early-response imaging biomarker for chemotherapy reflecting cell viability. Clin Cancer Res **2010**;16:212-25

31. Weidensteiner C, Allegrini PR, Sticker-Jantscheff M, Romanet V, Ferretti S, McSheehy PM. Tumour T1 changes in vivo are highly predictive of response to chemotherapy and reflect the number of viable tumour cells--a preclinical MR study in mice. BMC Cancer **2014**;14:88

32. Damadian R. Tumor detection by nuclear magnetic resonance. Science **1971**;171:1151-3

33. Hollis DP, Economou JS, Parks LC, Eggleston JC, Saryan LA, Czeister JL. Nuclear magnetic resonance studies of several experimental and human malignant tumors. Cancer Res **1973**;33:2156-60

34. Beall PT, Asch BB, Chang DC, Medina D, Hazlewood CF. Distinction of normal, preneoplastic, and neoplastic mouse mammary primary cell cultures by water nuclear magnetic resonance relaxation times. J Natl Cancer Inst **1980**;64:335-8

35. Beall PT, Hazlewood CF, Rao PN. Nuclear magnetic resonance patterns of intracellular water as a function of HeLa cell cycle. Science **1976**;192:904-7

36. Pauser S, Zschunke A, Khuen A, Keller K. Estimation of water content and water mobility in the nucleus and cytoplasm of Xenopus laevis oocytes by NMR microscopy. Magn Reson Imaging **1995**;13:269-76

37. Schoeniger JS, Aiken N, Hsu E, Blackband SJ. Relaxation-time and diffusion NMR microscopy of single neurons. J Magn Reson B **1994**;103:261-73

38. Franck JM, Ding Y, Stone K, Qin PZ, Han S. Anomalously Rapid Hydration Water Diffusion Dynamics Near DNA Surfaces. J Am Chem Soc **2015**;137:12013-23

39. Shimada H, Ambros IM, Dehner LP, Hata J, Joshi VV, Roald B*, et al.* The International Neuroblastoma Pathology Classification (the Shimada system). Cancer **1999**;86:364-72

40. Kerr JF, Wyllie AH, Currie AR. Apoptosis: a basic biological phenomenon with wide-ranging implications in tissue kinetics. Br J Cancer **1972**;26:239-57

41. Lambertz I, Kumps C, Claeys S, Lindner S, Beckers A, Janssens E*, et al.* Upregulation of MAPK Negative Feedback Regulators and RET in Mutant ALK Neuroblastoma: Implications for Targeted Treatment. Clin Cancer Res **2015**;21:3327-39

42. Berry T, Luther W, Bhatnagar N, Jamin Y, Poon E, Sanda T*, et al.* The ALK(F1174L) mutation potentiates the oncogenic activity of MYCN in neuroblastoma. Cancer Cell **2012**;22:117-30

43. Cazes A, Lopez-Delisle L, Tsarovina K, Pierre-Eugene C, De Preter K, Peuchmaur M*, et al.* Activated Alk triggers prolonged neurogenesis and Ret upregulation providing a therapeutic target in ALK-mutated neuroblastoma. Oncotarget **2014**;5:2688-702

44. Lopez-Delisle L, Pierre-Eugene C, Louis-Brennetot C, Surdez D, Raynal V, Baulande S*, et al.* Activated ALK signals through the ERK-ETV5-RET pathway to drive neuroblastoma oncogenesis. Oncogene **2018**

45. Gestblom C, Hoehner JC, Pahlman S. Proliferation and apoptosis in neuroblastoma: subdividing the mitosis-karyorrhexis index. Eur J Cancer **1995**;31A:458-63

46. DuBois SG, Mody R, Naranjo A, Van Ryn C, Russ D, Oldridge D*, et al.* MIBG avidity correlates with clinical features, tumor biology, and outcomes in neuroblastoma: A report from the Children's Oncology Group. Pediatr Blood Cancer **2017**;64

47. More SS, Itsara M, Yang X, Geier EG, Tadano MK, Seo Y*, et al.* Vorinostat increases expression of functional norepinephrine transporter in neuroblastoma in vitro and in vivo model systems. Clin Cancer Res **2011**;17:2339-49

48. Little RA, Jamin Y, Boult JKR, Naish JH, Watson Y, Cheung S*, et al.* Mapping Hypoxia in Renal Carcinoma with Oxygen-enhanced MRI: Comparison with Intrinsic Susceptibility MRI and Pathology. Radiology **2018**:171531

49. Heimlich JB, Speed JS, O'Connor PM, Pollock JS, Townes TM, Meiler SE*, et al.* Endothelin-1 contributes to the progression of renal injury in sickle cell disease via reactive oxygen species. Br J Pharmacol **2016**;173:386-95

50. Haller S, Zaharchuk G, Thomas DL, Lovblad KO, Barkhof F, Golay X. Arterial Spin Labeling Perfusion of the Brain: Emerging Clinical Applications. Radiology **2016**;281:337-56

51. Messiou C, Orton M, Ang JE, Collins DJ, Morgan VA, Mears D*, et al.* Advanced solid tumors treated with cediranib: comparison of dynamic contrast-enhanced MR imaging and CT as markers of vascular activity. Radiology **2012**;265:426-36

52. Aghighi M, Theruvath AJ, Pareek A, Pisani LL, Alford R, Muehe AM*, et al.* Magnetic Resonance Imaging of Tumor-Associated Macrophages: Clinical Translation. Clin Cancer Res **2018**;24:4110-8

53. Perrin J, Capitao M, Mougin-Degraef M, Guerard F, Faivre-Chauvet A, Rbah-Vidal L*, et al.* Cell Tracking in Cancer Immunotherapy. Front Med (Lausanne) **2020**;7:34

54. h-Ici DO, Jeuthe S, Al-Wakeel N, Berger F, Kuehne T, Kozerke S*, et al.* T1 mapping in ischaemic heart disease. Eur Heart J Cardiovasc Imaging **2014**;15:597-602

55. Schelbert EB, Messroghli DR. State of the Art: Clinical Applications of Cardiac T1 Mapping. Radiology **2016**;278:658-76

56. Pavlides M, Banerjee R, Sellwood J, Kelly CJ, Robson MD, Booth JC*, et al.* Multiparametric magnetic resonance imaging predicts clinical outcomes in patients with chronic liver disease. J Hepatol **2016**;64:308-15

57. Sado DM, Maestrini V, Piechnik SK, Banypersad SM, White SK, Flett AS*, et al.* Noncontrast myocardial T1 mapping using cardiovascular magnetic resonance for iron overload. J Magn Reson Imaging **2015**;41:1505-11

58. Wu WC, Jain V, Li C, Giannetta M, Hurt H, Wehrli FW*, et al.* In vivo venous blood T1 measurement using inversion recovery true-FISP in children and adults. Magn Reson Med **2010**;64:1140-7

Tables

Table 1. Summary of the response of the Th-*MYCN* transgenic model of neuroblastoma to vistusertib and alisertib.

A. Summary of the response of the Th-MYCN transgenic model of neuroblastoma to Vistusertib

	Vehicle control				**25mg/kg Vistusertib**			
	Pre	24h post	*Relative changes*	n	Pre	24h post	*Relative changes*	n
Tumor volume	1185±221mm^3	1474±245mm^3	*31±5.5%*	14	966±127 mm^3	577 ±93 mm^3 ***(<0.0001)*** §	*-42.0 ±5.1%* ***(<0.0001)*** ‡	12
T_1	1723 ±16ms	1771±14ms	*2.9±0.8%*	14	1712±25ms	1553±25ms ***(0.0001)*** §	*-9.3 ±0.9 %* ***(<0.0001)*** ‡	12
T_2	62±1ms	60±1ms	*-4.0±1.7 %*	14	63±2ms	58±2ms	*-8.0±2.7%*	12
R_2*	102±6s^{-1}	105 ±7s^{-1}	*4.5±3.3%*	14	99±6s^{-1}	113±10s^{-1}	*13.3 ±7.9%*	12
MTR	22.5±0.6%	22.3±0.4%	*-0.4 ±2.2%*	14	22.2±0.3%	23.0±0.5ms	*3.9±2.2%*	11
ADC	593 ±26 .10^{-6} mm^2.s^{-1}	569±22 .10^{-6} mm^2.s^{-1}	*-2.5±4.7%*	14	689±42 .10^{-6} mm^2.s^{-1}	686 ±40 .10^{-6} mm^2.s^{-1}	*2.4 ±8.6%*	10

B. Summary of the response of the Th-MYCN transgenic model of neuroblastoma to Alisertib

	Vehicle control				**30mg/kg Alisertib**			
	Pre	24h post	*Relative changes*	n	Pre	24h post	*Relative changes*	n
Tumor volume	781±176mm^3	981±198mm^3	*30.5±5.0%*	9	1037±109 mm^3	938 ±129 mm^3	*-11.2 ±4.3%* ***(<0.0001)*** ‡	11
T_1	1754 ±36ms	1750±32ms	*-0.2±0.6%*	9	1776±26ms	1679±21ms ***(0.0008)*** §	*-5.4±1.1 %* ***(<0.001)*** ‡	11
T_2	62±3ms	60±2ms	*-3.2±3.6 %*	6	62±1ms	63±1ms	*1.9±2.9%*	7
R_2*	109±14s^{-1}	117 ±20s^{-1}	*5.0±8.0%*	6	114±11s^{-1}	108±9s^{-1}	*-1.2 ±11.7%*	7
MTR	23.6±0.7%	22.3±1.0%	*-5.7 ±3.8%*	6	22.6±0.4%	21.5±0.5ms	*-0.37±3.2%*	7
ADC	664 ±66 .10^{-6} mm^2.s^{-1}	607 ±17 .10^{-6} mm^2.s^{-1}	*-5.6±6.3%*	6	615±29 .10^{-6} mm^2.s^{-1}	664 ±33 .10^{-6} mm^2.s^{-1}	*8.6 ±6.3%*	5

Data are presented as mean of tumor median value ± 1 s.e.m. § Student's two-tailed paired t-test, ‡ Student's two-tailed unpaired t-test, both incorporating a Bonferroni correction (n=6) and assuming a 1% level of significance. The difference in the number of mice associated with the different parameters reflects that it was not possible to acquire the full protocol in all cases.

Figure legends

Figure 1. Representative T_2-weighted anatomical MR images of tumor-bearing Th-*MYCN* mice and associated parametric maps of the tumor spin-lattice relaxation time T_1, transverse relaxation rate R_2*, spin-spin relaxation rate R_2 (=1/T_2), apparent diffusion coefficient (ADC) and magnetization transfer ratio (MTR), prior to and 24 hours following treatment with 25mg/kg vistusertib, 30mg/kg alisertib or vehicle.

Figure 2. A. Scatter graph of the native spin lattice relaxation time T_1 against native transverse relaxation rate R_2* from 71 untreated tumors arising in genetically-engineered murine models of neuroblastoma. Linear regression analysis and associated 95% confidence and prediction intervals are shown. A highly significant negative correlation was obtained (r = -0.59, P < 0.0001 with Bonferroni correction [n=5]). **B.** Box-and-whisker plot showing the difference in native T_1 in sub-regions categorized by low (<70s^{-1}), intermediate (70s^{-1}<R_2*<250s^{-1}) and high (>250s^{-1}) values of R_2* measured in Th-*MYCN* tumors treated with vehicle (n= 13). Data are medians and interquartile range. **C.** Scatter graph of relative changes in native tumor R_2* (ΔR_2*) and relative changes in native T_1 (ΔT_1) 24 hours following treatment with either alisertib or vistusertib. Bold lines represent linear regression with crossed dots indicating outliers determined using the robust regression and outlier removal approach. Grey shaded area indicates the 95% confidence intervals while dashed lines indicate 95% prediction confidence. A significant negative correlation was obtained (r = -0.78, P = 0.002 with Bonferroni correction [n=5]).

Figure 3. Computational analysis of a digitized whole-slide histological image of a Th-*MYCN* neuroblastoma. Cells were segmented and classified into 5 categories with an overall accuracy of 95.3% (50-fold cross-validation): undifferentiated neuroblasts (98.61% accuracy, green), differentiating neuroblasts (96.79%, purple), apoptotic cells (95.41%, yellow), lymphocytes (96.15%, blue), stromal cells (84.54%, red).

Figure 4. Representative MRI-derived parametric maps of the tumor spin-lattice relaxation time T_1 and transverse relaxation rate R_2*, and registered histopathology-derived parametric maps of cell density including undifferentiated and apoptotic neuroblasts in the Th-*MYCN* model of neuroblastoma, 24 hours following treatment with either vehicle control, 25mg/kg vistusertib or 30mg/kg alisertib.

Figure 5. A. Box-and-whisker plot showing the difference in native T_1 values in sub-regions categorized by low and high density of undifferentiated neuroblasts. Dichotomization was achieved using either median, Otsu or 85th percentile thresholds on registered histopathology-derived parametric maps of segmented and classified undifferentiated neuroblasts in vehicle control Th-*MYCN* tumors (n=13). **B.** Box-and-whisker plot showing the difference in undifferentiated neuroblast density in sub-regions categorized by low and high native T_1 values, defined using either median, Otsu or T_1>1900ms thresholds in vehicle control Th-*MYCN* tumors. Data are medians and interquartile range. (*P*, Wilcoxon signed rank test with a 5% level of significance) **C.** Proportion of undifferentiated and apoptotic neuroblasts relative to all cells derived from cell segmentation and classification from hematoxylin and eosin (H&E) stained histopathology from Th-*MYCN* tumors 24 hours following treatment with either vehicle control, 25mg/kg vistusertib or 30mg/kg alisertib. **D.** Scatter graph showing that the reduction in native tumor T_1 over 24h treatment with either alisertib or vistusertib correlated with an increased proportion of apoptotic cells present in the tumor at the time of excision (r= 0.55, *P*=0.04). **E,F.** Scatter graphs showing that median tumor native T_1 in the treated and vehicle control cohorts positively correlated with the proportion of undifferentiated neuroblasts (r= 0.70, *P*<0.0001), and negatively correlated with the proportion of apoptotic neuroblasts (r= -0.63, *P*=0.006). Grey shaded area indicates 95% confidence intervals while dashed lines indicate 95% prediction confidence.

Figure 6. Three cases of differentiating tumors in the Th-*MYCN* model of neuroblastoma. **A.** Representative MRI-derived parametric maps of the tumor spin-lattice relaxation time T_1 and transverse relaxation rate R_2*, and registered representative pathology-derived parametric maps of tumor cell density including undifferentiated, apoptotic and differentiated neuroblasts.

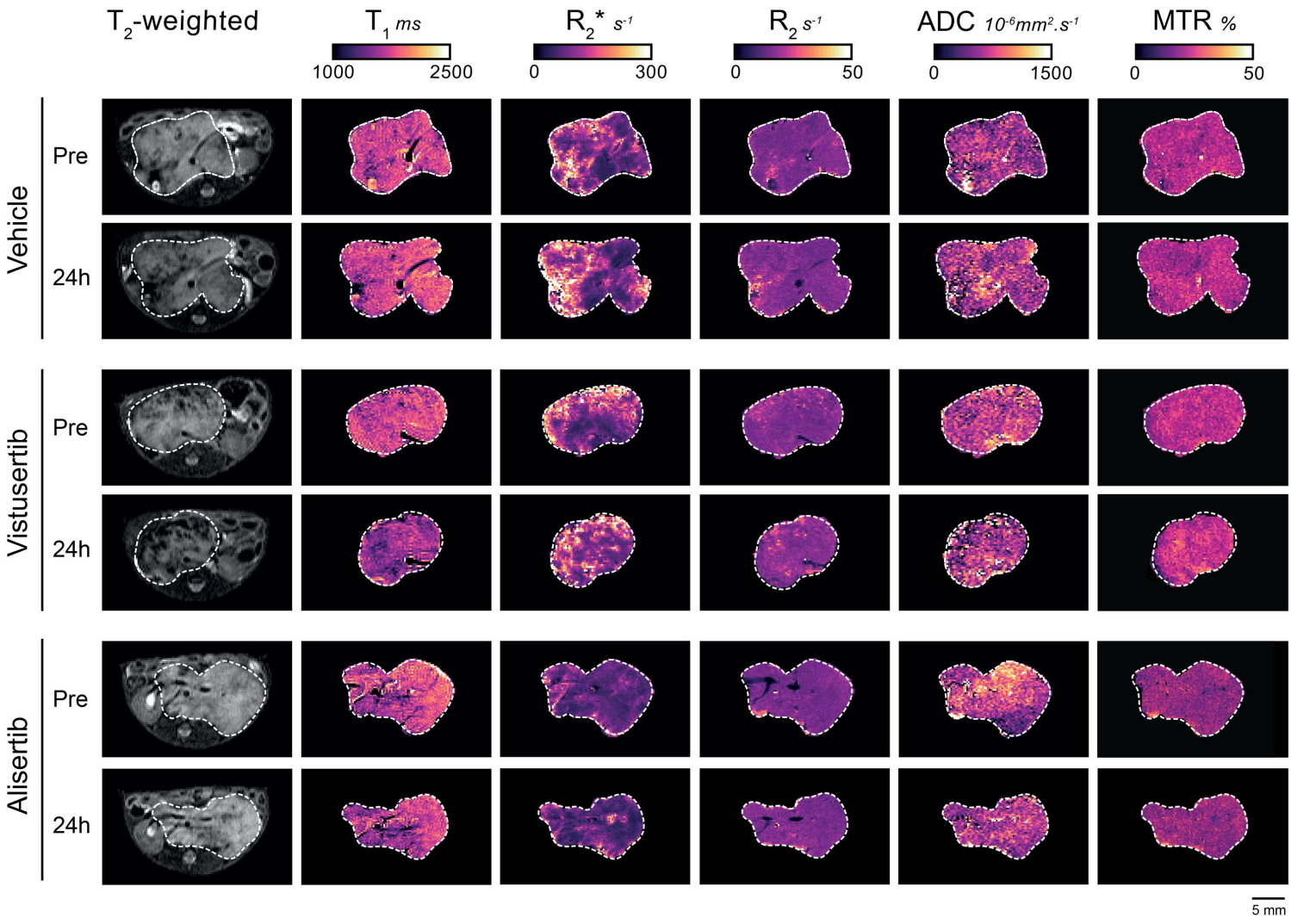
T2-weighted
T1 ms
1000
2500
R2* s-1
0
300
R2 s-1
0
50
ADC 10-6mm2.s-1
0
1500
MTR %
0
50
Vehicle
Pre
24h
Vistusertib
Pre
24h
Alisertib
Pre
24h
5 mm

Figure 1

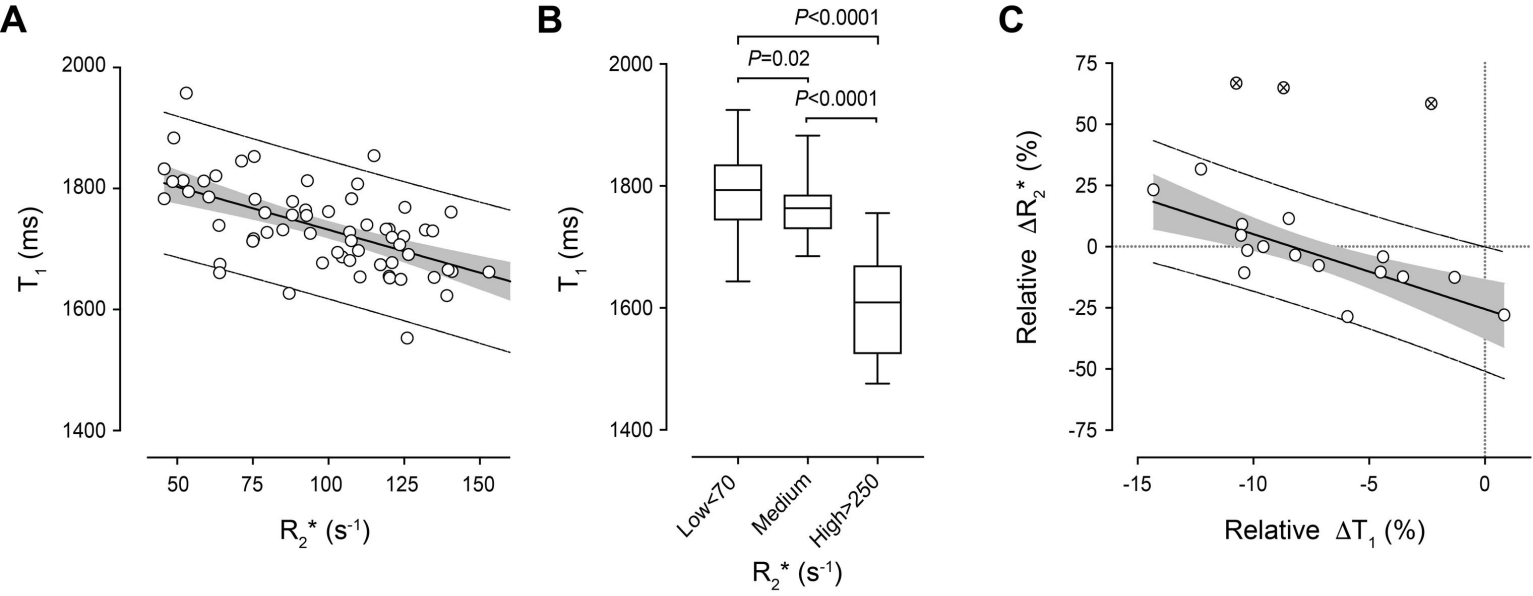
A
2000
1800
1600
1400
T1 (ms)
50
75
100
125
150
R2* (s-1)
B
P<0.0001
P=0.02
P<0.0001
2000
1800
1600
1400
T1 (ms)
Low<70
Medium
High>250
R2* (s-1)
C
75
50
25
0
-25
-50
-75
Relative ΔR2* (%)
-15
-10
-5
0
Relative ΔT1 (%)

Figure 2

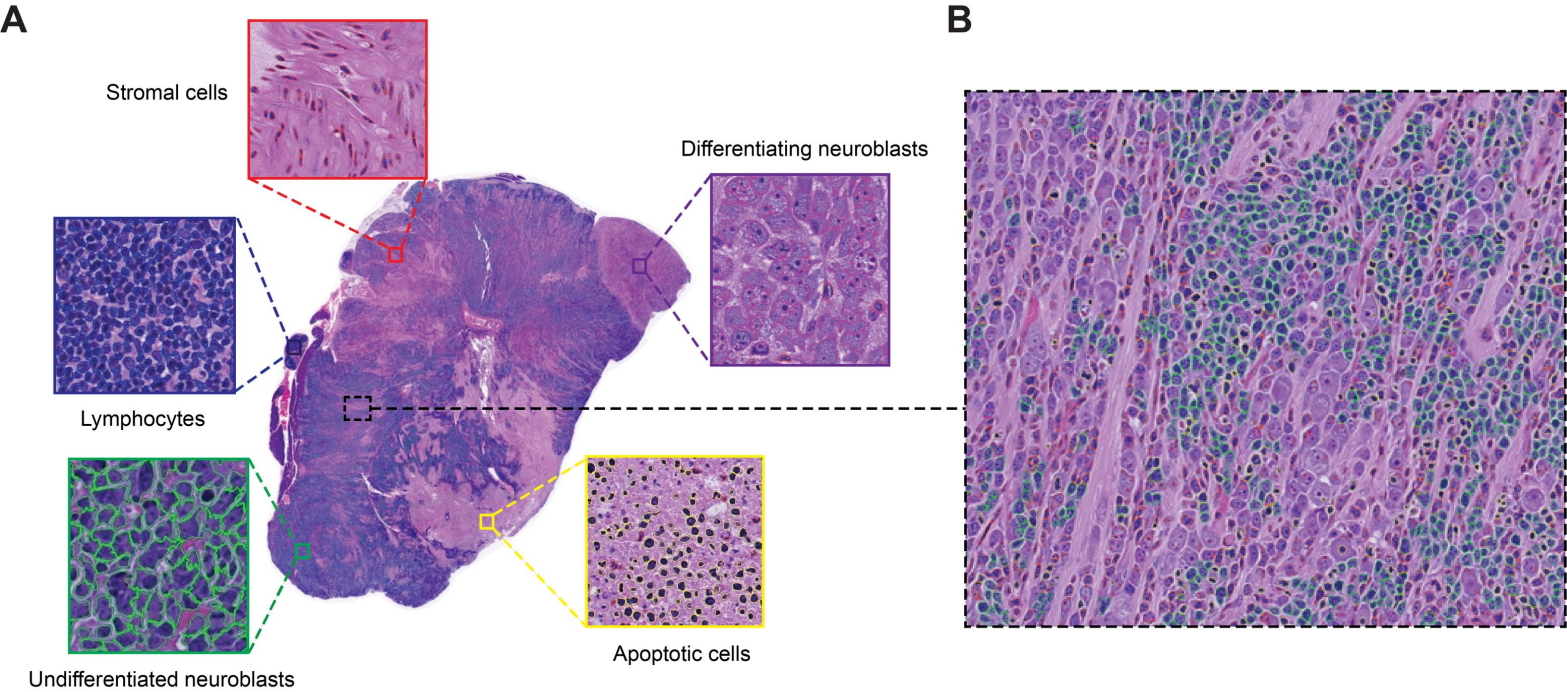
A
B
Stromal cells
Differentiating neuroblasts
Lymphocytes
Undifferentiated neuroblasts
Apoptotic cells

Figure 3

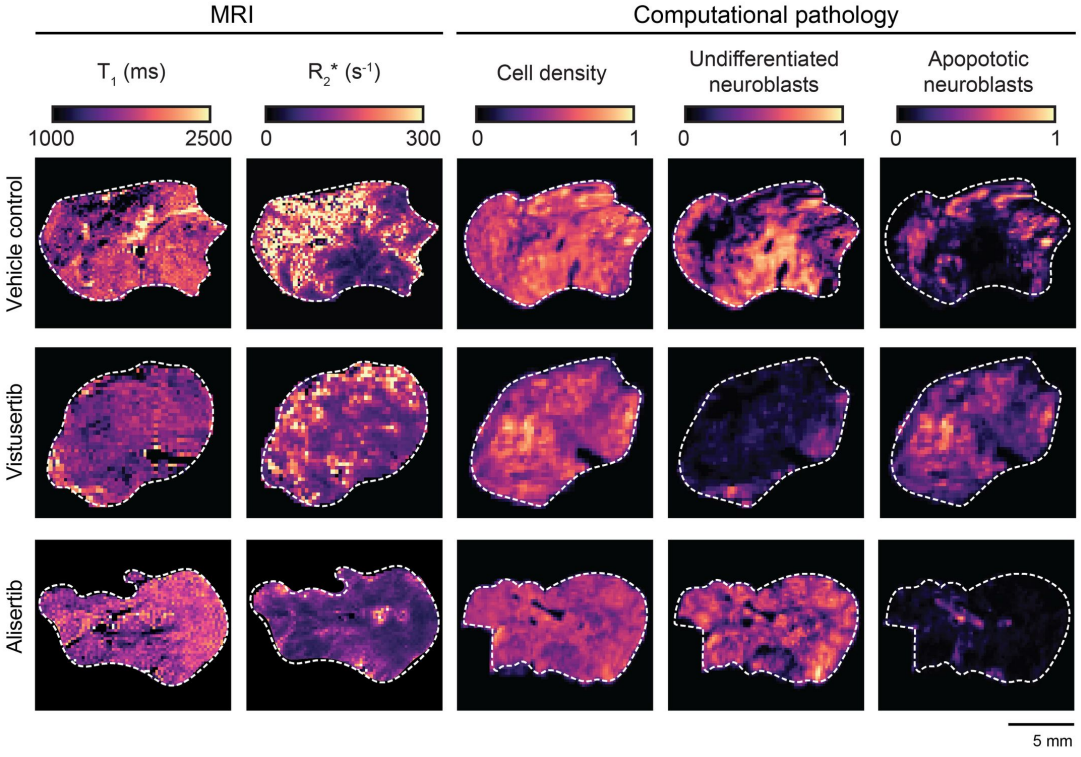
MRI
Computational pathology
T1 (ms)
R2* (s-1)
Cell density
Undifferentiated neuroblasts
Apopototic neuroblasts
1000
2500
0
300
0
1
0
1
0
1
Vehicle control
Vistusertib
Alisertib
5 mm

Figure 4

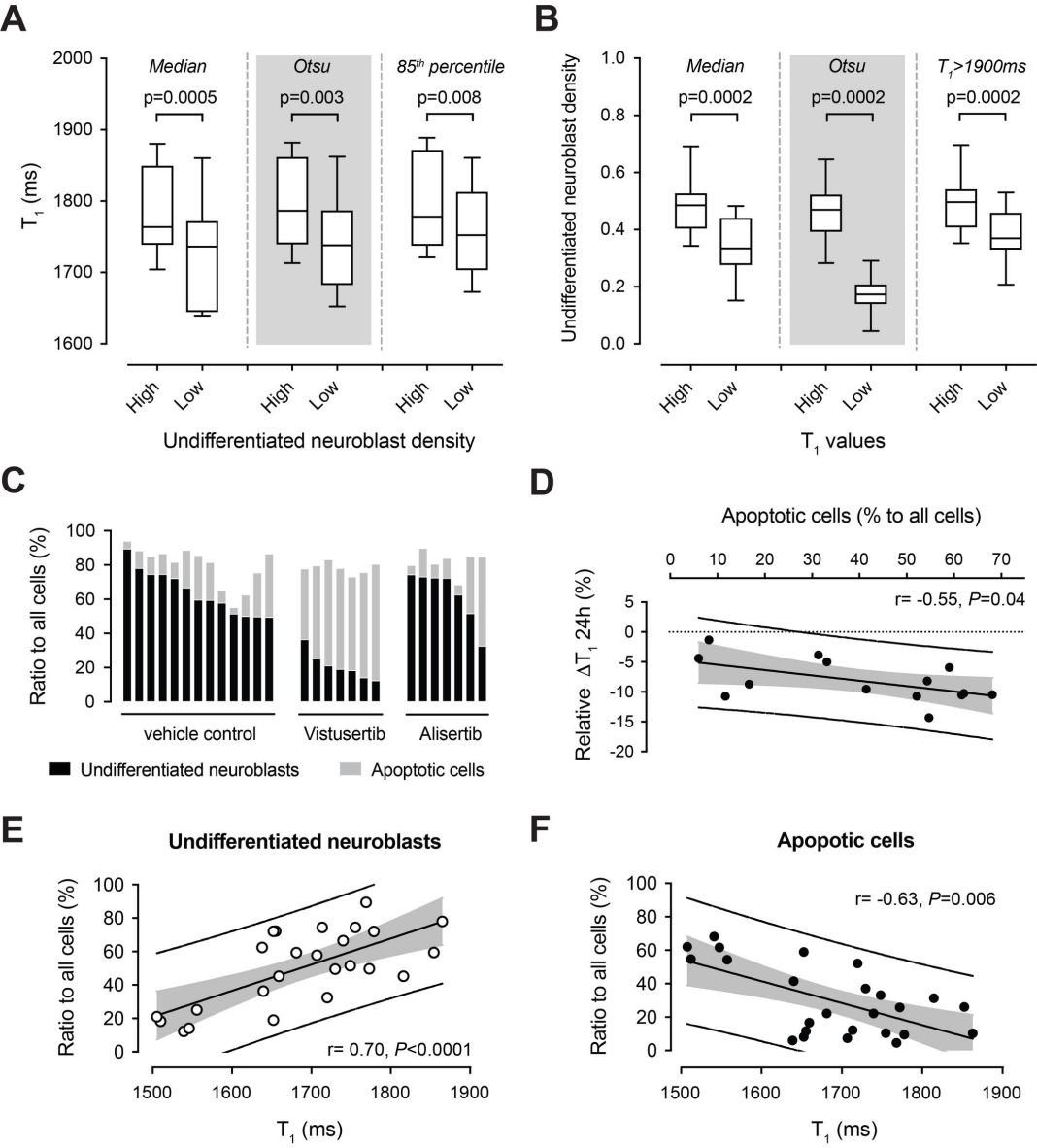
A
Median
Otsu
85th percentile
p=0.0005
p=0.003
p=0.008
T1 (ms)
2000
1900
1800
1700
1600
High
Low
Undifferentiated neuroblast density
B
Median
Otsu
T1>1900ms
p=0.0002
p=0.0002
p=0.0002
Undifferentiated neuroblast density
1.0
0.8
0.6
0.4
0.2
0.0
T1 values
C
Ratio to all cells (%)
vehicle control
Vistusertib
Alisertib
Undifferentiated neuroblasts
Apoptotic cells
D
Apoptotic cells (% to all cells)
r= -0.55, P=0.04
Relative ΔT1 24h (%)
E
Undifferentiated neuroblasts
r= 0.70, P<0.0001
T1 (ms)
F
Apopotic cells
r= -0.63, P=0.006

Figure 5

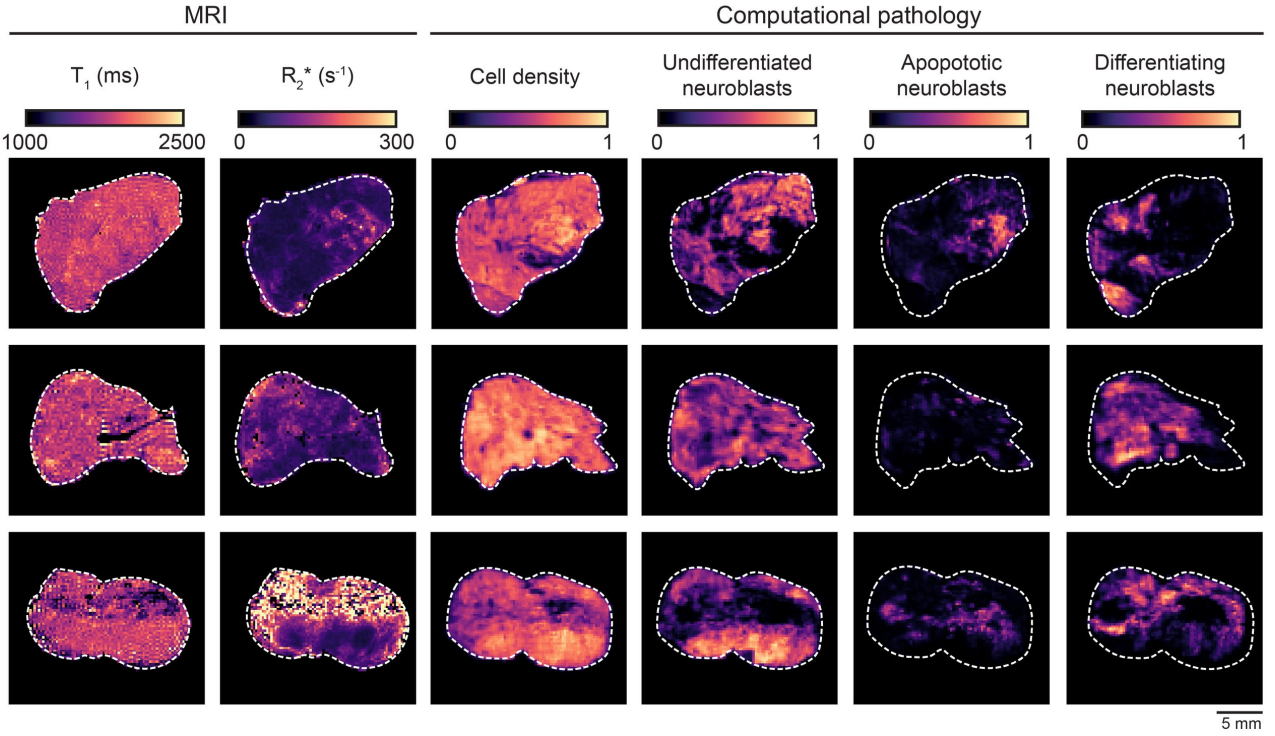
MRI
Computational pathology
T1 (ms)
R2* (s-1)
Cell density
Undifferentiated neuroblasts
Apopototic neuroblasts
Differentiating neuroblasts
1000
2500
0
300
0
1
0
1
0
1
0
1
5 mm

Figure 6